Green Chemistry

PAPER

View Article Online
View Journal | View Issue



Cite this: *Green Chem.*, 2026, **28**, 1235

# MOF-derived cobalt catalysts for sustainable tandem hydroformylation–acetalization in green solvents: experimental and DFT calculations

Wejdan Hadi Anbari, †[a] Leandro Duarte Almeida,†[a] Alejandra Rendón Patiño,[a] Rafia Ahmad,[b] Luis Garzon-Tovar,[a] Luigi Cavallo [b] and Jorge Gascon *[a]

The development of efficient and sustainable catalysts for multi-step transformations is central to advancing green chemistry. Herein, we report a non-noble metal tandem catalytic system for the hydroformylation–acetalization of alkenes, combining atom economy with operational simplicity. The catalyst was obtained by pyrolysis of crystalline ZIF-67, yielding cobalt nanoparticles embedded in a nitrogen-doped carbon matrix (Co@$C_{600}$). This non-noble metal catalyst enables the one-pot transformation of alkenes to acetals using syngas and alcohols under relatively mild conditions (140 °C and 50 bar). The use of an environmentally benign solvent mixture of anisole with methanol proved essential for maximizing acetal yields and selectivity. Density functional theory (DFT) calculations revealed that nitrogen incorporation into the carbon support enhances aldehyde adsorption within the ideal energy range for catalytic turnover, explaining the superior activity observed. The system exhibited excellent recyclability and maintained high selectivity across terminal, internal, and cyclic alkenes. This work highlights the potential of earth-abundant metals and tandem catalytic strategies in developing greener synthesis of oxygenated fine chemicals.

Received 26th August 2025,
Accepted 7th December 2025

DOI: 10.1039/d5gc04496k

rsc.li/greenchem



### Green foundation

1. This work demonstrates the first heterogeneous, cobalt-based catalyst capable of performing tandem hydroformylation–acetalization of alkenes under mild conditions (140 °C, 50 bar) in environmentally benign solvent mixtures such as anisole and methanol, eliminating the need for noble metals or acid co-catalysts.
2. The catalyst, Co@C600, is obtained by scalable pyrolysis of ZIF-67 to yield cobalt nanoparticles embedded in nitrogen-doped porous carbon. This system delivers high conversion, acetal selectivity (up to 89%), and recyclability across a broad substrate scope, including terminal, internal, and cyclic olefins. DFT studies show that nitrogen doping tunes aldehyde adsorption into the optimal energy window for turnover, providing a mechanistic design principle for green tandem catalysis.
3. Further greening could be achieved by employing renewable feedstocks, reducing syngas pressure and temperature, and implementing continuous-flow processes to minimize energy input and maximize catalyst efficiency.

## Introduction

Tandem or cascade transformations have emerged as a powerful strategy in modern catalysis, offering key advantages such as improved efficiency, reduced waste generation, and enhanced atom economy.[1–5] These sequential reactions, carried out in a single reaction vessel, also eliminate the need for laborious and wasteful purification steps that consume chemicals and time.[6,7] Despite these advantages, tandem processes can be challenging to implement due to the need for compatible catalysts, reagents, and reaction conditions, as well as the risk of undesired side reactions.[6] Nevertheless, this approach holds significant promise for the fine chemical industry,[8] where value-added compounds are typically prepared in multiple sequential steps.

Acetal production represents a key area in fine chemical synthesis, as these compounds serve as versatile intermediates for pharmaceuticals,[9–11] fragrances,[12–14] and diesel additives.[15–17] Typically, acetals are prepared *via* the acid-catalysed reaction of aldehydes with alcohols. In recent years, sustainable approaches to acetal synthesis have been explored through

[a]*Advanced Catalytic Materials (ACM), KAUST Catalysis Center (KCC), King Abdullah University of Science and Technology (KAUST), Thuwal 23955-6900, Saudi Arabia. E-mail: jorge.gascon@kaust.edu.sa*
[b]*KAUST Catalysis Center (KCC), King Abdullah University of Science and Technology (KAUST), Thuwal 23955-6900, Saudi Arabia*
† These authors contributed equally to this work.

tandem hydroformylation–acetalization processes. Most reported systems rely on noble-metal homogeneous catalysts such as Rh,[18–20] Ir,[21,22] and Ru,[23] often in combination with acid co-catalysts (Scheme 1, top). A limited number of heterogeneous systems has also been described, generally involving the immobilization of rhodium complexes onto solid supports.[24–29] To the best of our knowledge, no reports to date have demonstrated the use of heterogeneous, non-noble metal-based catalysts for this transformation.

The design of tailored heterogeneous catalysts offers a promising approach for enabling tandem reactions by promoting individual transformations at specific active sites.[30–34] Bifunctional – or multifunctional – materials, presenting distinct catalytic sites, can facilitate each step of a reaction sequence, enabling the efficient formation of the desired product. Metal–organic frameworks (MOFs) and their derived materials have emerged as particularly attractive platforms for designing such catalysts due to their highly tunable structures. Among them, ZIF-67, a cobalt-based MOF, has received considerable attention as a precursor for non-noble-metal heterogeneous catalysts. Upon pyrolysis, ZIF-67 yields nitrogen-doped carbon-supported cobalt materials that exhibit enhanced catalytic properties. In recent years, cobalt-based heterogeneous catalysts have shown growing promise in hydroformylation reactions.[35–42] Indeed, both our group and Jiang's group have recently demonstrated the hydroformylation of olefins using these cobalt-derived materials.[43,44] However, the application of such earth-abundant heterogeneous catalysts in tandem transformations remains unexplored.

In this work, we report the first tandem hydroformylation–acetalization of olefins catalysed by a heterogeneous, non-noble-metal-based system (Scheme 1, bottom). This earth-abundant bifunctional catalyst enables both C–C bond formation and subsequent acetalization in a single reaction vessel, under mild conditions and without the use of homogeneous metal complexes or additional acid co-catalysts. Our findings not only demonstrate the feasibility of this sustainable transformation but also offer a promising alternative for streamlined fine chemical synthesis. Furthermore, mechanistic insights supported by density functional theory (DFT) calculations are provided to elucidate the nature of the active sites and the reaction pathway, offering a deeper understanding of the catalytic behaviour and selectivity. These results underscore the potential of earth-abundant catalysts for sustainable tandem catalysis, combining practical efficiency with fundamental mechanistic understanding.

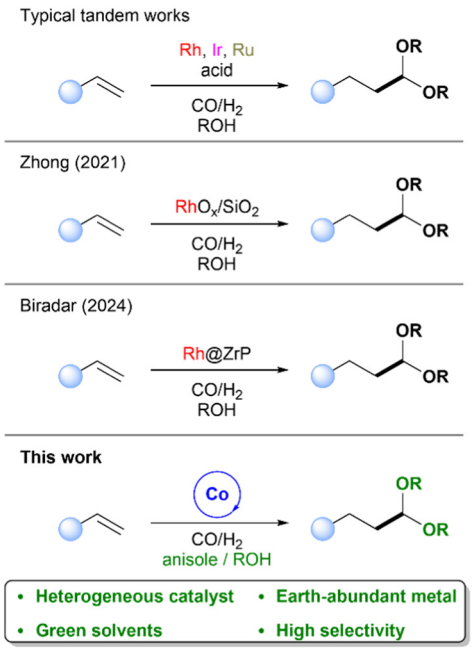


**Scheme 1** Tandem hydroformylation–acetalization.

## Experimental

### General information

All the chemicals were obtained from commercial sources and used as received unless otherwise stated. The $CO:H_2$ gas mixture presented a 1 : 1 ratio. Gas chromatography (GC) analysis was performed in an Agilent 7890A equipped with an HP-5MS (10 m × 0.10 mm internal diameter) column using an FID detector. The GC coupled with mass spectrometry (GC-MS) analysis were conducted in an Agilent 5977B MSD equipment using an electron ionization (EI) detector equipped with a DB-5MS column (60 m × 0.25 mm internal diameter). Information about the characterizations of the fresh and used materials can be found in the SI.

### Synthesis of ZIF-67

ZIF-67 was synthesized following a literature procedure with slight modifications.[45] In a 500 mL beaker flask, $Co(NO_3)_2{\cdot}6H_2O$ (3.240 g) was dissolved in methanol (160 mL). Separately, 2-methylimidazole (7.4 g) was dissolved in methanol (160 mL) in another flask and then added to the cobalt solution. The resulting solution was stirred at room temperature for 24 hours. Subsequently, the synthesized product was subjected to centrifugation and washed with methanol until the centrifuged liquid turned colourless, then filtered and dried under vacuum at 150 °C overnight.

### Pyrolysis of ZIF-67

The pyrolysis process was conducted using a quartz tubular reactor positioned vertically within a tube furnace. ZIF-67 was placed inside the reactor, and with a continuous flow of $N_2$ (30 mL $min^{-1}$), it was subjected to heating at 600 °C for 6 hours at a heating rate of 2 °C $min^{-1}$. After cooling down below 50 °C, the materials were passivated under a flow of air (20 mL $min^{-1}$) for 2 hours.

### Tandem hydroformylation–acetalization experiments

The tandem reactions were conducted using a H.E.L. High Pressure Chem-SCAN II reactor fitted with 16 mL 316 stainless steel vessels. In a typical procedure, substrate (2 mmol), cata-

lyst (25 mg), solvent (total volume 5 mL), and mesitylene (0.1 mL) as the internal standard were combined in a glass vial before being introduced into the reactor. The reactor was initially purged with $N_2$ (2 × 10 bar), followed by pressurization with $CO:H_2$, and then heated to the desired temperature. Carbon monoxide is a highly toxic gas, and hydrogen is flammable. All reactions were performed in high-pressure autoclaves equipped with safety relief valves, inside a ventilated fume hood, and with continuous gas-leak monitoring. Upon cooling and depressurization, the resulting mixture was filtered through a syringe filter (0.45 μm), and the liquid phase was subjected to analysis *via* GC. For recycling experiments, the used catalyst was thoroughly washed with acetone and dried at room temperature before being reintroduced into a fresh reaction mixture. Liquid products were further characterized by GC-MS, and spectroscopic data were compared with the reference databank. Conversion and yield were determined as follows:

$$\text{Conversion } (\%) = \left(\frac{\text{mmol substrate}_{0\,\text{h}} - \text{mmol substrate}_{x\,\text{h}}}{\text{mmol substrate}_{0\,\text{h}}}\right) \times 100$$

$$\text{Yield } (\%) = \left(\frac{\text{mmol acetals}_{x\,\text{h}}}{\text{mmol substrate}_{0\,\text{h}}}\right) \times 100$$

### DFT methodology

All calculations were performed using spin-polarized density functional theory (DFT) as implemented in the Vienna *Ab initio* Simulation Package (VASP version (5.4.4)). The Perdew–Burke–Ernzerhof (PBE) exchange–correlation functional was employed in combination with Grimme's D3 dispersion correction (PBE-D3) to account for long-range van der Waals interactions.[46,47] Projector augmented-wave (PAW) pseudopotentials were used with a plane-wave kinetic energy cutoff of 500 eV. Due to the large supercell dimensions, Γ-point or 3 × 3 × 1 Monkhorst–Pack k-point sampling was deemed sufficient. Structural optimizations were considered converged when the total energy change was below $10^{-5}$ eV and the maximum atomic force was below 0.02 eV $Å^{-1}$. Adsorption energies ($E_{ads}$) of nonanal and 2-methyloctanal were computed according to the expression:

$$E_{ads} = E_{system} - E_{support+cluster} - E_{adsorbate}$$

where $E_{system}$ is the total energy of the optimized adsorbate–cluster–support complex, $E_{support+cluster}$ is the energy of the clean supported cluster, and $E_{adsorbate}$ is the energy of the isolated aldehyde molecule in vacuum. Negative values of $E_{ads}$ correspond to exothermic adsorption.

To investigate the influence of nitrogen doping on catalytic performance, we modelled the adsorption of aldehydes on Co and CoO nanoparticles supported on three distinct carbon-based materials: (i) pristine graphene, (ii) nitrogen-doped graphene with isolated graphitic nitrogen (CN), and (iii) porous graphitic carbon nitride (pCN), a defect-rich, nitrogen-rich extended 2D material with periodic porosity.

The **graphene** substrate was represented by a 9 × 9 supercell (162 carbon atoms) with periodic boundary conditions and a vacuum spacing of 10 Å along the *z*-direction. For the **CN** model, a single carbon atom in the graphene lattice was replaced with nitrogen, simulating an isolated graphitic N dopant. The **pCN** support was constructed as a 3 × 3 supercell of a porous $C_3N_4$ monolayer based on experimentally reported frameworks.[48,49] This material reflects the highly nitrogen-doped and defect-rich nature of pyrolyzed MOF-derived carbon supports.

Cobalt and cobalt oxide nanoparticles were modelled as approximately spherical clusters (~1 nm diameter, ~80 atoms). The Co clusters were built in a compact, close-packed metallic configuration, while CoO clusters were constructed with rock-salt-like oxygen coordination. These clusters were placed on the supports in low-energy orientations, ensuring multiple points of contact with the surface. Adsorbates (nonanal and 2-methyloctanal) were introduced such that their carbonyl oxygen coordinated directly to the exposed Co or CoO atoms at the metal–support interface.

The systematic comparison across the three support types—graphene, CN, and pCN—enabled a detailed analysis of how nitrogen content and local defect structures influence aldehyde adsorption. These models are consistent with experimentally relevant catalyst structures derived from ZIF-67 pyrolysis and align with recent reports on bifunctional, nitrogen-doped carbon-supported metal catalysts.[50,51] All geometries were optimized prior to energy evaluation to ensure accurate thermodynamic characterization. The completely optimized geometries of all the models are included in Fig. S8 and S9.

## Results and discussion

ZIF-67 was synthesized following a previously established procedure (Fig. 1a).[45] Characterization of the activated material by powder X-ray diffraction (PXRD) (Fig. S1a), scanning electron microscopy (SEM) (Fig. 1b), thermogravimetric analysis (Fig. S1b), and nitrogen adsorption analysis ($S_{BET}$ = 1498 $m^2$ $g^{-1}$, Fig. S1c and d) confirmed the successful formation of phase-pure, dodecahedral ZIF-67 crystals with an average particle size of 321 ± 70 nm (Fig. S1e and f).

Subsequently, ZIF-67 was pyrolyzed at 600 °C for 6 hours under a nitrogen atmosphere to obtain the material $Co@C_{600}$, as illustrated in Fig. 1a. As known, the thermal treatment of ZIF-67 under an inert atmosphere produces cobalt nanoparticles embedded in a carbon matrix, which is attributed to the partial decomposition of the organic linker.[52] This pyrolysis temperature was selected based on the optimized conditions established in our previous study on hydroformylation.[44] As expected, the powder X-ray diffraction (PXRD, Fig. 1c) pattern and transmission electron microscopy (TEM) images (Fig. 1b and S2) of the obtained material confirmed the formation of metallic cobalt ($Co^0$) nanoparticles, with an average particle size of 5.6 ± 2.7 nm (Fig. 1b inlet). Furthermore, high-angle annular dark-field scanning trans-

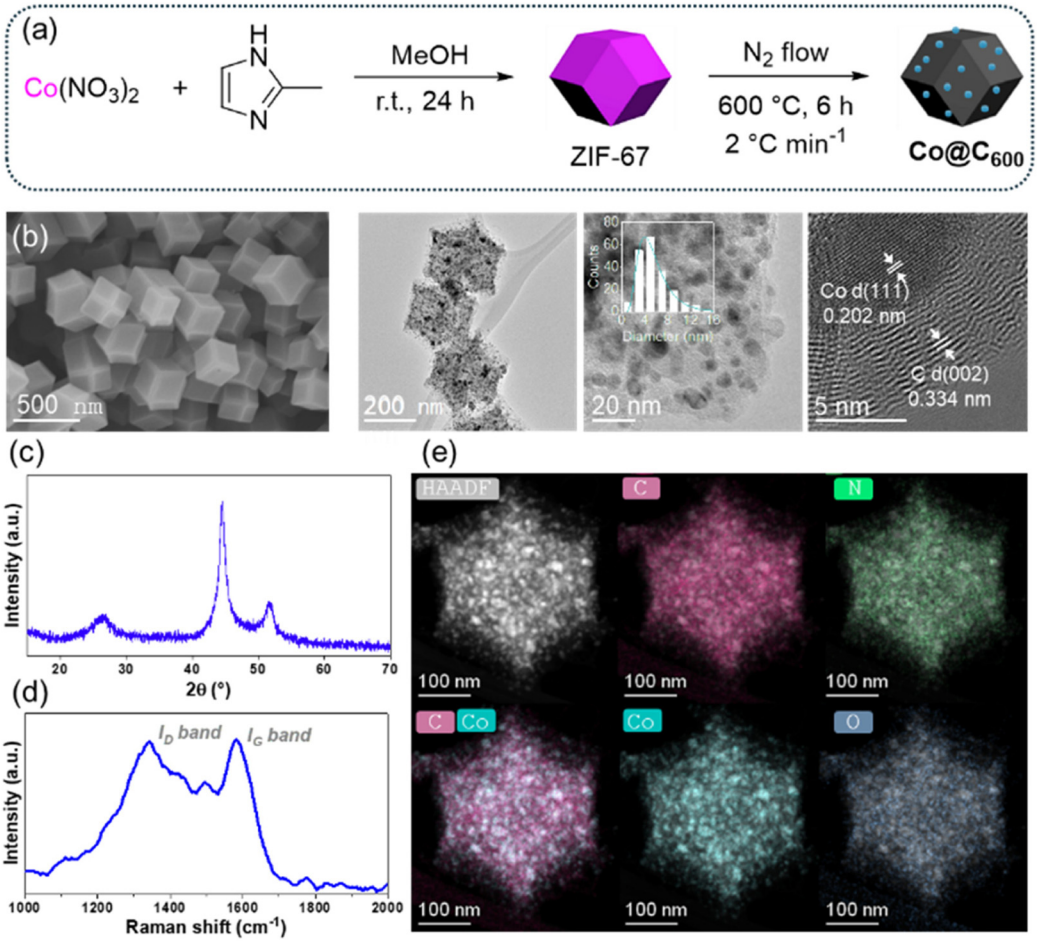


**Fig. 1** (a) Catalyst preparation, (b) SEM image of pristine ZIF-67, (c) XRD, (d) Raman, and (e) high-angle annular dark-field scanning transmission electron microscopy of $Co@C_{600}$.

mission electron microscopy (HAADF-STEM) coupled with energy-dispersive X-ray spectroscopy (EDX) demonstrated that the cobalt nanoparticles are uniformly dispersed within the nitrogen-doped carbon matrix (Fig. 1e and Fig. S3). A cobalt content of 36% was determined by thermogravimetric analysis (TGA) in air (Fig. S4), while CHN elemental analysis revealed the carbon, nitrogen, and hydrogen contents, as summarized in Table S1. The porosity and degree of graphitization of the carbon matrix were evaluated by nitrogen adsorption analysis and Raman spectroscopy, respectively. $Co@C_{600}$ exhibited a BET-specific surface area of 298 $m^2\ g^{-1}$ (Fig. S5) and an $I_D/I_G$ ratio of 0.98 (Fig. 1d), characteristic of partially graphitized carbon materials, both consistent with previously reported values.[44,53]

The analysis using XPS spectroscopy provides detailed information about the surface composition of the material (Fig. S6 and Tables S2–4). The C 1s spectrum reveals characteristic peaks of C=C (284.4 eV, 51.8%) and C–C bonds (285.3 eV, 25.4%), indicating a graphitic structure on the surface, consistent with the results obtained by Raman spectroscopy. The surface also has functional groups like C=N/C–N (286.1 eV, 8.7%), C–O (286.8 eV, 5.4%), and C=O (287.7 eV, 3.4%), suggesting a high density of defects, typical for materials made by pyrolysing ZIF-67. The nitrogen spectrum shows that nitrogen is mainly in pyridinic (398.1 eV, 21.8%), pyrrolic (398.8 eV, 38.5%), and graphitic (400.0 eV, 39.6%) forms. Regarding cobalt, the Co 2p spectrum reveals the presence of different oxidation states, as indicated by the presence of satellites. The deconvolution of the Co $2p_{3/2}$ peak shows a peak corresponding to Co(0) (778.0 eV, 18.0%), while oxidized species of Co(III) (780.1 eV, 14.1%) and Co(II) (780.8 eV, 11.8%) are also observed. These oxidized forms result from a controlled passivation treatment.[54–56] The acidity of the oxidized cobalt sites was investigated by $NH_3$-TPD, as shown in Fig. S7. Peak deconvolution suggests the presence of weak (159 and 202 °C) and medium-strength acid sites (284 °C). A similar desorption profile has been reported for iron-based MOF-derived catalysts,[57] demonstrating that the pyrolysis approach is effective for generating bifunctional catalysts that combine metallic and weak acidic sites.

Scheme 2 illustrates the complexity of tandem hydroformylation–acetalization pathways. In addition to the desired reac-

 

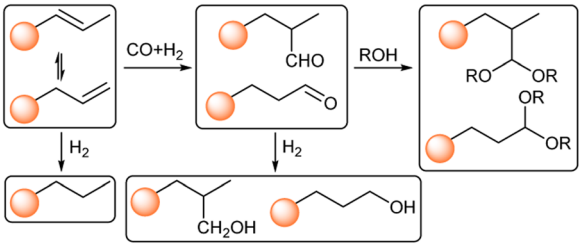


**Scheme 2** Reaction pathways for tandem hydroformylation–acetalization.

tion sequence, olefin isomerization typically occurs, while still contributing to branched acetal formation. Conversely, aldehyde hydrogenation to the corresponding alcohol is an undesired side reaction, lowering atom efficiency and reducing the overall selectivity for acetal products. We started our tandem catalysis investigation using 1-octene (**1**) and methanol as model reaction, aiming to synthesize the corresponding branched and linear acetals (**1a**/**1a**′). However, under reaction conditions of 140 °C and 50 bar of $CO/H_2$ in pure methanol, the use of $Co@C_{600}$ did not result in the formation of any oxygenated products. As previously shown, the use of polar solvents can dramatically hinder the hydroformylation activity using pyrolyzed ZIF-67 as catalyst.[44] To overcome this limitation, we prepared various mixtures of anisole and methanol while maintaining a constant total solvent volume, as shown in Fig. 2. Under similar reaction conditions of pressure and temperature, GC-MS analysis revealed the formation of four distinct acetal isomers, along with the corresponding intermediate aldehydes (**1b**)—attributed to double-bond isomerization of the starting olefin—as well as other by-products.

We observed that increasing the amount of methanol in the mixture led to a higher overall yield of acetals. Specifically, acetal yields of 80% and 82% were obtained with anisole : methanol ratios of 2.5 : 2.5 and 1.0 : 4.0 mL, respectively. Likewise, aldehyde selectivity decreased from 13% to 3%, indicating that higher methanol availability promotes more efficient *in situ* acetalization. In contrast, at the highest anisole content (4.5 : 0.5 mL), the acetal yield was moderate (41%), accompanied by significant amounts of aldehydes (28%) and other by-products (28%). Notably, the linear-to-branched (l/b) ratio of the acetal products decreased with increasing methanol content, suggesting that the cobalt catalyst system promotes the isomerization to branched olefins under more protic and polar conditions. At the highest anisole content (4.5 : 0.5 mL), the l/b ratio reached a maximum of 3.1, whereas at 1.0 : 4.0 mL, it decreased to 0.8.

Once the anisole/methanol ratio was optimized, we investigated the effects of co-solvent, reaction temperature, and syngas pressure on the tandem hydroformylation/acetalization of 1-octene (Table S5). Initially, a set of renewable solvents—anisole, *p*-cymene, and dimethyl carbonate—along with toluene, the benchmark solvent, were selected based on relevant solvents guides and literature reviews (entries 1–4).[58–61]

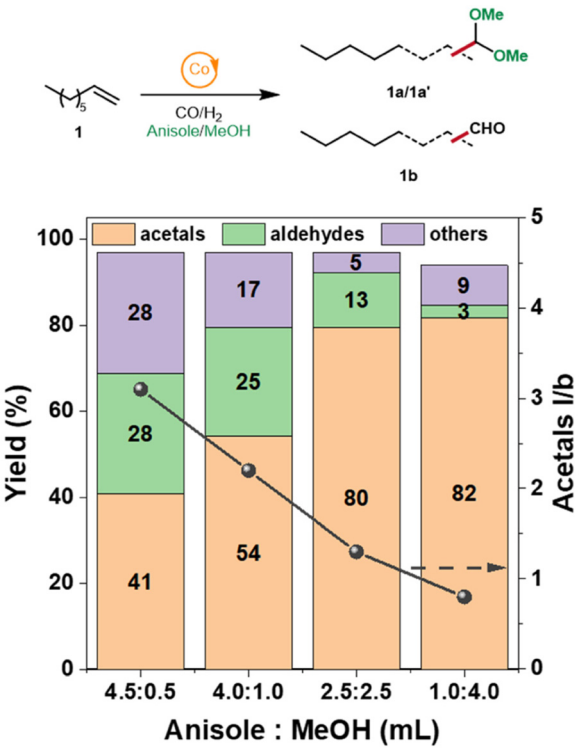


**Fig. 2** Solvent mixture optimization in the tandem acetals reaction. Conditions: 1-octene (2 mmol), $Co@C_{600}$ (25 mg), anisole : methanol (5 mL total volume), $CO/H_2$ (50 bar), 140 °C, 18 h. Conversion and yield were determined by GC using mesitylene as the internal standard. Acetals l/b refers to the ratio of linear to branched acetals.

Among these, anisole significantly outperformed the other solvents, achieving 96% conversion and 81% yield of the target acetals (**1a**/**1a**′, entry 3). In contrast, toluene, *p*-cymene, and dimethyl carbonate afforded slightly lower conversions and yields (90–83% conversion, 69–74% yield). These results suggest a beneficial effect of anisole's moderate polarity compared to the lower polarity of toluene and *p*-cymene, and the higher polarity of dimethyl carbonate. The similar l/b ratios observed across these entries (0.82–0.89) indicate that regioselectivity is primarily governed by the intrinsic properties of the catalyst rather than solvent effects under these conditions.

Subsequent experiments varying temperature and pressure (entries 5–7) confirmed 140 °C and 50 bar as optimal conditions. Reducing the pressure from 50 to 30 bar led to a notable decrease in both conversion (96%–84%) and acetal yield (81%–60%), indicating that syngas pressure is crucial for maintaining hydroformylation activity (entries 3, 5 and 6). Additionally, lowering the temperature to 130 °C significantly diminished substrate conversion and acetals formation (entry 7). Experiments varying 1-octene concentration (Fig. S8) showed a linear correlation with the reaction rate, consistent with first-order kinetics. This behaviour aligns with previous reports on heterogeneous rhodium-catalysed hydroformylation.[62,63] Furthermore, monitoring the isomerization of 1-octene into internal octenes at different substrate

concentrations revealed an almost constant ratio between 1-octene and internal octenes after 2 and 4 hours (Fig. S8b), suggesting a first-order dependence with respect to the olefin isomerization.

Kinetic isotope effect (KIE) experiments were performed to compare the reaction kinetics in $CH_3OH$ and $CD_3OD$ (Fig. S9). The isomerization of 1-octene into internal octenes proceeded more slowly in deuterated methanol than in regular methanol. Similarly, the formation of acetals was reduced when $CD_3OD$ was used. Moreover, a higher l/b ratio of acetals was observed in the deuterated solvent, which can be attributed to the slower formation of internal octenes. Regarding the rate-limiting step, the aldehyde intermediates remained at low concentrations throughout the reaction—even in deuterated methanol—consistent with their rapid conversion into acetals. The absence of aldehyde accumulation indicates that the overall reaction rate is governed by the hydroformylation of olefins, whereas the subsequent acetalization step proceeds relatively quickly.

To verify the heterogeneous nature of the cobalt catalyst, a hot filtration experiment was conducted (Fig. S10a). After the catalyst removal, no further catalytic activity was observed in the filtrate, confirming the structural stability of the synthesized Co@$C_{600}$. To probe the role of acidic sites, control reactions were carried out using commercial CoO and $Co_3O_4$ with either 1-octene or nonanal as substrates (Table S5, entries 8–11). The experiments were performed using equal content of cobalt compared to Co@$C_{600}$. While CoO showed activity in both transformations, it was unstable under the reaction conditions, as evidenced by a marked colour change indicative of cobalt leaching. In contrast, $Co_3O_4$, containing both Co(II) and Co(III), was active only in the acetalization of nonanal, with no hydroformylation observed for 1-octene.

To properly assess the effect of nitrogen sites, cobalt MOF-74 was synthesized and subsequently pyrolyzed (for experimental details, see the SI). It is important to note that the organic linker 2,5-dihydroxyterephthalic acid used to synthesize this MOF contains no nitrogen atoms. PXRD confirmed the formation of the desired pristine MOF (Fig. S11a). After pyrolysis, PXRD and TEM analyses revealed the formation of metallic cobalt nanoparticles (Fig. S11b–f), with an average particle size of 6.2 ± 0.9 nm—comparable to that observed for the Co@$C_{600}$ catalyst. Catalytic tests showed higher activity than Co@$C_{600}$ under identical conditions (Table S5, entries 12 and 13), but a visible colour change suggested cobalt leaching. This was confirmed by a hot-filtration experiment (Fig. S10b), demonstrating that pyrolyzed Co-MOF-74 lacks stability under hydroformylation conditions and highlighting the critical role of nitrogen sites in stabilizing cobalt in Co@$C_{600}$.

Under the optimal reaction conditions, we monitored the evolution of 1-octene conversion and product selectivity over time (Fig. 3a). Rapid substrate consumption was observed within the first 4 h, reaching 61% conversion, followed by a gradual increase to a plateau of 94% conversion at 18 h. Acetal selectivity remained remarkably stable throughout the reaction, ranging from 85–89%. This consistency suggests that the acetalization step proceeds in parallel and at a rate comparable to hydroformylation, reflecting efficient tandem coupling without significant aldehyde accumulation. Interestingly, the l/b ratio remained nearly constant over time. However, the ratio between 1-octenes and isomerized octenes indicates a preference for the formation of branched olefins (Fig. 3b). This observation implies that reversible isomerization toward 1-octene regeneration occurs during the reaction, likely contributing to the maintenance of a stable l/b product ratio.

To evaluate the effect of nitrogen doping on the catalytic performance of Co/CoO nanoparticles supported on carbon materials, we performed DFT calculations on the adsorption of nonanal and 2-methyloctanal. We modeled 1 nm Co and CoO clusters supported on three surfaces: (i) pristine graphene, (ii) nitrogen-doped graphene containing isolated graphitic nitrogen (CN), and (iii) a porous carbon nitride sheet (pCN) (Fig. S12 and S13). These models enable us to decouple geometric confinement from electronic effects induced by nitrogen. The CN model represents dilute nitrogen doping analogous to edge pyridinic/pyrrolic sites in carbon supports obtained during ZIF-67 pyrolysis, while the pCN model mimics a nitrogen-rich framework, reflecting the experimentally observed transition from carbon to N-rich carbonaceous domains upon extended pyrolysis.[50,51]

The computed adsorption energies for nonanal and 2-methyloctanal are summarized in Fig. 3d. For nonanal, CoO–graphene exhibits weak interaction with a slightly endothermic adsorption energy of +0.10 eV. Nitrogen doping enhances binding significantly: −0.23 eV on CoO–CN and −0.34 eV on CoO–pCN. A similar trend was seen for Co clusters: from −0.58 eV on graphene to −0.59 eV on CN and −0.68 eV on pCN. For 2-methyloctanal, adsorption is even stronger. CoO–graphene shows nearly non-interacting behavior (−0.03 eV), while CoO–CN and CoO–pCN yield −0.45 eV and −0.77 eV, respectively. Co–graphene gives −0.84 eV, improving to −1.04 eV on CN and −1.14 eV on pCN, the strongest interaction observed. These results indicate that nitrogen incorporation in the support systematically strengthens aldehyde adsorption on both Co and CoO nanoparticles, with porous pCN being most effective.

To understand the electronic origin of this trend, we examined the projected density of states (PDOS) of the supported Co and CoO clusters (Fig. S14 and S15). Nitrogen doping induces a redistribution of electronic density at the metal–support interface, shifting Co 3d states closer to the Fermi level. This results in increased overlap with the O 2p lone-pair orbitals of the aldehydes, as seen by enhanced DOS intensity near Fermi level upon adsorption. The effect is most pronounced for CN and pCN, where hybridization between adsorbate states and Co 3d orbitals is stronger; confirming that nitrogen coordination increases the Lewis acidity of surface Co sites and promotes binding of oxygenated intermediates. Thus, PDOS analysis supports the conclusion that nitrogen modifies Co electronically rather than purely structurally.

To quantify charge redistribution, Bader charge analysis was performed for the CN-supported systems, because they

 

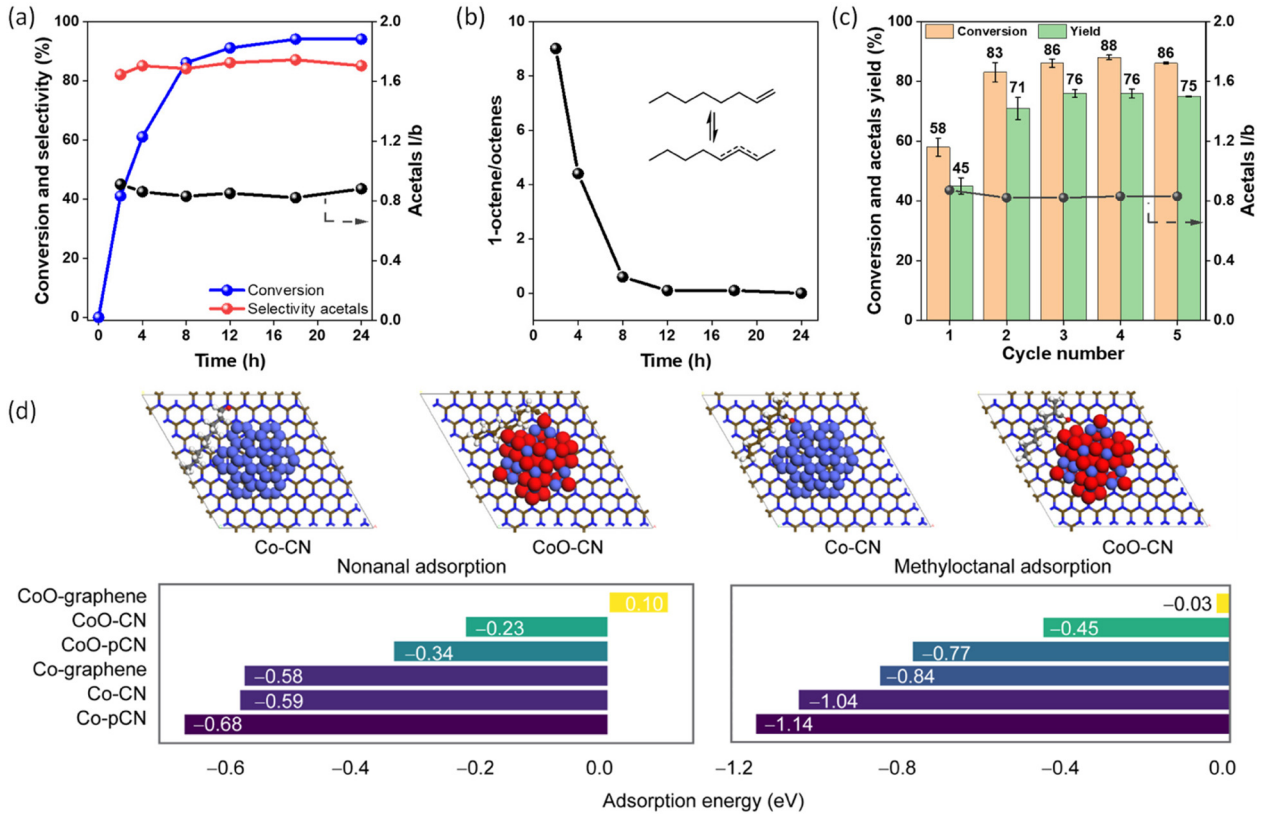


**Fig. 3** (a and b) Kinetic profile of the tandem 1-octene hydroformylation/acetalization, reuse of Co@$C_{600}$ catalyst, and (d) Adsorption energies of nonanal (left) and 2-methyloctanal (right) on 1 nm Co and CoO nanoparticles supported on graphene, N-doped graphene (CN), and porous carbon nitride (pCN) surfaces computed from DFT. The top panel shows representative optimized adsorption geometries for Co–CN and CoO–CN, where aldehydes adsorb *via* the carbonyl oxygen on surface-exposed metal sites. Adsorption energies (in eV) are given relative to gas-phase aldehydes and clean supported clusters; negative values indicate exothermic adsorption. The atom colors in the adsorption geometries are as follows: cobalt atoms are shown in blue, oxygen atoms from the CoO cluster and aldehyde carbonyl groups are shown in red, carbon atoms in the support and adsorbates appear in grey/light brown, nitrogen atoms in the CN support are highlighted in dark blue, and hydrogen atoms are shown in white. Conditions: 1-octene (2 mmol), Co@$C_{600}$ (25 mg), anisole : methanol (1 : 4 mL), CO/$H_2$ (50 bar), 140 °C, 4 h for (c). Conversion and selectivity were determined by GC using mesitylene as the internal standard. Acetals l/b refers to the ratio of linear to branched acetals.

best reflect the experimentally relevant nitrogen environment (Fig. S16). Only minor charge transfer from the aldehyde oxygen to the Co surface (0.03–0.05 |e|) was observed, indicating that adsorption is not driven by strong ionic charge transfer but rather by orbital hybridization, consistent with chemisorption through the carbonyl oxygen. Although Bader charge analysis alone does not fully explain the observed trends, it confirms localized charge polarization at the adsorption site, while the PDOS captures the dominant electronic structure effects of nitrogen.

From a catalytic perspective, aldehyde adsorption is a key step in tandem hydroformylation–acetalization, as surface-bound intermediates must remain adsorbed long enough to couple with methanol.[12,26] Literature suggests optimal adsorption energies between −0.5 and −1.5 eV,[64,65] balancing sufficient surface residence time with product desorption. The Co/CoO–pCN systems fall within this regime, indicating that nitrogen-doped supports achieve electronic tuning of aldehyde affinity into a catalytically relevant window. Overall, these results demonstrate that nitrogen doping enhances aldehyde adsorption on Co and CoO *via* electronic interaction rather than purely geometrical effects, validating the experimentally observed promotional role of nitrogen-doped supports.

The recyclability of the catalyst Co@$C_{600}$ was evaluated using the model reaction of 1-octene with anisole : methanol for 4 hours (Fig. 3c). After the first run, the catalytic system exhibited a marked increase in both conversion and acetal yield, reaching a plateau in subsequent cycles. Specifically, the conversion increased from 58% in the first cycle to 83–86% from the second cycle onward. A similar trend was observed in the acetals yield, which increased from 45% in the first cycle to approximately 71–76% in subsequent runs. The formation of coke on the catalyst surface was discarded, as the TGA analysis of fresh and used catalyst displayed the same profile (Fig. S17a). The Raman spectra and $I_G/I_D$ bands ratio are in agreement with this finding (Fig. S17b). After the fifth reaction cycle, the catalyst was analysed using TEM, STEM high-resolution mapping, and XPS to better understand the factors behind the enhancement in catalytic performance. TEM analysis revealed that the size of the cobalt nanoparticles

Table 1 Substrate scope of the tandem catalysed reaction[a]

| Entry | Substrate | Alcohol | Conv. (%)[b] | Sel. acetals (%)[b] | Sel. aldehydes (%)[b] | Sel. others (%)[b] | Acetals l/b[c] |
|---|---|---|---|---|---|---|---|
| 1 | 1-Octene | MeOH | 97 | 83 | 5 | 12 | 0.88 |
| 2 | *trans*-2-Octene | MeOH | 97 | 84 | 5 | 11 | 0.80 |
| 3 | *trans*-4-Octene | MeOH | 97 | 82 | 6 | 12 | 0.73 |
| 4 | 1-Hexene | MeOH | 99 | 83 | 1 | 16 | 1.20 |
| 5 | Cyclohexene | MeOH | 98 | 89 | 2 | 9 | n.a. |
| 6 | Cyclohexene | EtOH | >99 | 37 | 36 | 27 | n.a. |
| 7 | Cyclohexene | iPrOH | >99 | 1 | 61 | 38 | n.a. |

[a] Substrate (2 mmol), Co@$C_{600}$ (25 mg), anisole : alcohol (1.0 : 4.0 mL), 140 °C, $CO/H_2$ (50 bar), 24 h. [b] Conversion and selectivity were determined by GC using mesitylene as internal standard. [c] Acetals l/b refers to the ratio of linear to branched acetals.

remained unchanged (5.4 ± 2.5 nm) (Fig. S18 and S19), while STEM mapping showed an increase in localized oxygen content on the cobalt particles (Fig. S20). This result was confirmed by XPS, which showed a decrease in Co0 (13.6%) and an increase in Co(II) (19.9%) compared to the fresh sample (Table S6 and Fig. S21). The increase in surface cobalt oxides likely promotes acetalization activity by providing more Lewis acidic sites, which can facilitate substrate activation and stabilize reaction intermediates.

In addition, the XPS results showed a significant increase in cobalt site exposure (4.3%) relative to the fresh catalyst. This observation aligns with our previous findings,[44] where we proposed that enhanced exposure of cobalt active sites during reaction cycles contributes to the overall improvement in catalytic performance. Interestingly, the linear-to-branched (l/b) ratio of the acetals remained relatively stable across all cycles, fluctuating only slightly between ~0.80–0.86. This observation suggests that the electronic changes associated with mild oxidation of the cobalt surface do not significantly impact the regioselectivity of the tandem transformation. The O 1s spectrum reveals four distinct components (Table S7 and Fig. S22). Upon catalyst use, the intensity of the lattice Co–O peak decreases, while the contribution associated with Co–OH and defective oxygen species increases, consistent with the higher proportion of $Co^{2+}$ observed in the Co 2p region. These changes indicate that the cobalt surface evolves from a thin oxide layer to a more hydroxylated and defect-rich state dominated by $Co^{2+}$ species.

Finally, the robustness of the tandem hydroformylation/acetalization strategy was further demonstrated through a substrate scope evaluation (Table 1). To investigate the influence of double bond position on catalytic performance, 1-octene, *trans*-2-octene, and *trans*-4-octene were evaluated under standard conditions. While all substrates achieved high conversions (97%), the l/b acetal ratio progressively decreased from 1-octene (0.88) to 2-octene (0.80) and 4-octene (0.73) (entries 1–3). These results suggest that olefins isomerization affects the regioselectivity of the hydroformylation step, likely due to differences in insertion geometry and steric hindrance. Notably, acetal selectivity remained constantly high (≥82%) across the octenes series, demonstrating that the tandem sequence proceeds efficiently despite changes in regioselectivity.

Further insight into the substrate scope was obtained using 1-hexene and cyclohexene (entries 4 and 5). 1-Hexene, a shorter terminal alkene, exhibited excellent conversion (99%) and high acetal selectivity (83%), along with a significantly higher l/b ratio (1.20), highlighting the system's preference for linear aldehyde formation from smaller terminal substrates. Cyclohexene, a cyclic internal alkene lacking terminal isomerization possibilities, also showed high conversion (98%) and excellent acetal selectivity (89%) when methanol was used. Changing the alcohol from methanol to ethanol or isopropanol led to notable shifts in product distribution (entries 5–7). With ethanol, acetal selectivity dropped to 37%, accompanied by increased aldehydes and by-products formation. Using isopropanol, the reaction yielded only trace amounts of acetal (1%), with aldehydes (61%) and by-products (38%) dominating. The by-products refer to the hydrogenation of the olefins to the respective alkanes or to the aldehyde hydrogenation to the respective alcohol. These results suggest that alcohol bulkiness and nucleophilicity strongly influence the efficiency of the tandem process.

## Conclusions

This work presents a sustainable tandem catalytic system based on a non-noble cobalt catalyst supported on nitrogen-doped carbon for the one-pot hydroformylation–acetalization of industrially relevant alkenes. The tandem approach eliminates the need for intermediate purification steps, improving atom economy and overall process efficiency. The catalyst Co@$C_{600}$, derived from ZIF-67 *via* pyrolysis, combines the advantages of using an earth-abundant metal with the structural benefits of *N*-doped porous carbon supports. Under optimized conditions, 80% yield for acetals was obtained with an l/b 0.88 regioselectivity. Interestingly, internal olefins such as *trans*-2-octene and 4-octene presented similar yields and regioselectivity. Solvent optimization using anisole enabled high conversion and selectivity under relatively mild conditions for heterogeneous hydroformylation. DFT studies revealed that nitrogen doping significantly enhances aldehyde adsorption within the optimal energy range, promoting efficient acetal formation without compromising catalyst turnover. The system displayed excellent recyclability and broad substrate applica-

 

bility, maintaining high activity and selectivity across five cycles. These findings underscore the potential of designing non-precious metal catalysts in green tandem processes, contributing to more sustainable fine chemical synthesis.

## Author contributions

Conceptualization: W.H.A., and L.D.A. Methodology: W.H.A., L.D.A., A.R.P., R.A., and L.G.T. Validation: W.H.A., and R.A. Formal analysis: R.A., and L.C. Investigation: W.H.A., L.D.A., A. R.P., and L.G.T. Resources: L.C., and J.G. Writing – original draft: L.D.A., A.R.P., R.A., and L.G.T. Writing – review & editing: L.C., and J.G. Supervision: L.C., and J.G. Funding acquisition: L.C., and J.G.

## Conflicts of interest

There are no conflicts to declare.

## Data availability

The data supporting this article have been included as part of the supplementary information (SI).

Supplementary information is available. See DOI: https://doi.org/10.1039/d5gc04496k.

## Acknowledgements

Funding for this work was provided by King Abdullah University of Science and Technology (KAUST). L.C. acknowledges the KAUST Supercomputing Laboratory for providing computational resources for the supercomputer Shaheen III.

## References

1 H. J. Cho and B. Xu, *Trends Chem.*, 2020, **2**, 929–941.
2 K. C. Nicolaou, D. J. Edmonds and P. G. Bulger, *Angew. Chem., Int. Ed.*, 2006, **45**, 7134–7186.
3 L. F. Tietze, G. Brasche and K. M. Gericke, *Domino Reactions in Organic Synthesis*, Wiley, 2006.
4 J.-C. Wasilke, S. J. Obrey, R. T. Baker and G. C. Bazan, *Chem. Rev.*, 2005, **105**, 1001–1020.
5 J. Zhu and H. Bienaymé, Eds., *Multicomponent Reactions*, Wiley, 2005.
6 S. Schmidt, K. Castiglione and R. Kourist, *Chem. – Eur. J.*, 2018, **24**, 1755–1768.
7 J. Zhou, *Chem. – Asian J.*, 2010, **5**, 422–434.
8 B. P. Bondžić, *J. Mol. Catal. A: Chem.*, 2015, **408**, 310–334.
9 Y.-J. Wu and N. A. Meanwell, *J. Med. Chem.*, 2021, **64**, 9786–9874.
10 R. Gannimani, P. Walvekar, V. R. Naidu, T. M. Aminabhavi and T. Govender, *J. Controlled Release*, 2020, **328**, 736–761.
11 A. Mattarei, M. Azzolini, M. Carraro, N. Sassi, M. Zoratti, C. Paradisi and L. Biasutto, *Mol. Pharm.*, 2013, **10**, 2781–2792.
12 C. G. Vieira, E. N. dos Santos and E. V. Gusevskaya, *Appl. Catal., A*, 2013, **466**, 208–215.
13 C. G. Vieira, J. G. da Silva, C. A. A. Penna, E. N. dos Santos and E. V. Gusevskaya, *Appl. Catal., A*, 2010, **380**, 125–132.
14 M. C. de Freitas, C. G. Vieira, E. N. dos Santos and E. V. Gusevskaya, *ChemCatChem*, 2013, **5**, 1884–1890.
15 I. Agirre, M. B. Güemez, A. Ugarte, J. Requies, V. L. Barrio, J. F. Cambra and P. L. Arias, *Fuel Process. Technol.*, 2013, **116**, 182–188.
16 A. R. Trifoi, P. Ș. Agachi and T. Pap, *Renew. Sustain. Energy Rev.*, 2016, **62**, 804–814.
17 E. García, M. Laca, E. Pérez, A. Garrido and J. Peinado, *Energy Fuels*, 2008, **22**, 4274–4280.
18 Y.-Q. Li, P. Wang, H. Liu, Y. Lu, X.-L. Zhao and Y. Liu, *Green Chem.*, 2016, **18**, 1798–1806.
19 Z. Shu, X.-X. Zhao, Z. Zheng, X. Zhang, Y. Zhang, S. Sun, J. Chen, C. Xie, B. Yuan and X. Jia, *Chem. Commun.*, 2023, **59**, 5237–5240.
20 B. El Ali, J. Tijani and M. Fettouhi, *J. Mol. Catal. A: Chem.*, 2005, **230**, 9–16.
21 H. Liu, L. Liu, W.-D. Guo, Y. Lu, X.-L. Zhao and Y. Liu, *J. Catal.*, 2019, **373**, 215–221.
22 H. Liu, Y.-X. Yao, H.-Y. Shang, D. Yang and Y.-Y. Tian, *React. Chem. Eng.*, 2023, **8**, 778–783.
23 C. Rodrigues, F. G. Delolo, J. Norinder, A. Börner, A. L. Bogado and A. A. Batista, *J. Mol. Catal. A: Chem.*, 2017, **426**, 586–592.
24 A. S. Singh, H. G. Kachgunde, K. Ravi, D. R. Naikwadi and A. V. Biradar, *Mol. Catal.*, 2024, **555**, 113859.
25 F. M. S. Rodrigues, L. D. Dias, M. J. F. Calvete, T. M. R. Maria, L. M. Rossi, A. J. L. Pombeiro, L. M. D. R. S. Martins and M. M. Pereira, *Catalysts*, 2021, **11**, 608.
26 X. Li, T. Qin, L. Li, B. Wu, T. Lin and L. Zhong, *Catal. Lett.*, 2021, **151**, 2638–2646.
27 D. N. Gorbunov, T. V. Shchukina, Y. S. Kardasheva, N. A. Sinikova, A. L. Maksimov and E. A. Karakhanov, *Pet. Chem.*, 2016, **56**, 711–716.
28 Z. Shu, X. Zhang, W. Meng, Z. Yu, Y. Zhou, C. Chen, B. Yuan and X. Jia, *ACS Sustainable Chem. Eng.*, 2024, **12**, 2430–2438.
29 B. El Ali, J. Tijani and M. Fettouhi, *Appl. Catal., A*, 2006, **303**, 213–220.
30 Y.-B. Huang, J. Liang, X.-S. Wang and R. Cao, *Chem. Soc. Rev.*, 2017, **46**, 126–157.
31 D. Jagadeesan, *Appl. Catal., A*, 2016, **511**, 59–77.
32 F. Zaera, *Chem. Rev.*, 2022, **122**, 8594–8757.
33 M. J. Climent, A. Corma, S. Iborra and M. J. Sabater, *ACS Catal.*, 2014, **4**, 870–891.
34 C. Xie, Z. Niu, D. Kim, M. Li and P. Yang, *Chem. Rev.*, 2020, **120**, 1184–1249.
35 C. Galdeano-Ruano, S. Gutiérrez-Tarriño, C. W. Lopes, J. Mazarío, L. E. Chinchilla, G. Agostini, J. J. Calvino,

J. Pedro Holgado, E. Rodríguez-Castellón, A. Roldan and P. Oña-Burgos, *J. Catal.*, 2024, 115374.
36 J. Ti, K. Gong, D. Cui, Y. An, T. Lin and L. Zhong, *Catal. Sci. Technol.*, 2024, **14**, 885–893.
37 Z. Pu, J. Zhao, H. Yin, J. Zhao, X. Ma and J. Zeng, *Nano Lett.*, 2024, **24**, 852–858.
38 W. Gao, S. Liu, Z. Wang, J. Peng, Y. Zhang, X. Yuan, X. Zhang, Y. Li and Y. Pan, *Energy Fuels*, 2024, **38**, 2526–2547.
39 B. Wei, J. Chen, X. Liu, K. Hua, L. Li, S. Zhang, H. Luo, H. Wang and Y. Sun, *Cell Reports Phys. Sci.*, 2022, **3**, 101016.
40 H. Gong, X. Zhao, Y. Qin, W. Xu, X. Wei, Q. Peng, Y. Ma, S. Dai, P. An and Z. Hou, *J. Catal.*, 2022, **408**, 245–260.
41 W. Xu, Y. Ma, X. Wei, H. Gong, X. Zhao, Y. Qin, Q. Peng and Z. Hou, *New J. Chem.*, 2022, **46**, 15712–15722.
42 B. Wei, X. Liu, Y. Deng, K. Hua, J. Chen, H. Wang and Y. Sun, *ACS Catal.*, 2021, **11**, 14319–14327.
43 S. Hu, X. Dong, J. Tian, L. Wang, Y. Chen and H. Jiang, *ChemistrySelect*, 2023, **8**, e202303025.
44 L. D. Almeida, A. R. Patiño, J. L. Cerrillo, S. Telalovic, L. Garzon–Tovar and J. Gascon, *ChemCatChem*, 2025, **17**, e202401482.
45 Y. Chen, C. Wang, Z. Wu, Y. Xiong, Q. Xu, S. Yu and H. Jiang, *Adv. Mater.*, 2015, **27**, 5010–5016.
46 S. Grimme, J. Antony, S. Ehrlich and H. Krieg, *J. Chem. Phys.*, 2010, **132**, 154104.
47 J. P. Perdew, K. Burke and M. Ernzerhof, *Phys. Rev. Lett.*, 1996, **77**, 3865–3868.
48 Y. Wang, X. Wang and M. Antonietti, *Angew. Chem., Int. Ed.*, 2012, **51**, 68–89.
49 K. Peramaiah, V. Ramalingam, H. Fu, M. M. Alsabban, R. Ahmad, L. Cavallo, V. Tung, K. Huang and J. He, *Adv. Mater.*, 2021, **33**, 2100812.
50 Y. Long, S. Li, P. Yang, X. Chen, W. Liu, X. Zhan, C. Xue, D. Liu and W. Huang, *Sep. Purif. Technol.*, 2022, **286**, 120470.
51 Y. Wu, Y. Wang, Z. Xiao, M. Li, Y. Ding and M. Qi, *RSC Adv.*, 2021, **11**, 2693–2700.
52 A. de A. Lourenço and F. F. da Silva, *Heterogeneous Catalysis*, Elsevier, 2022, pp. 471–495.
53 A. Sousa, A. Rendón-Patiño, L. Garzon-Tovar, D. Mateo, J. Gascon and A. Bavykina, *ChemSusChem*, 2025, **18**, e202401896.
54 Q. Gao, G. Li, G. Kofie, B. Chen and F. Yin, *Carbon Lett.*, 2024, **34**, 951–960.
55 B. Lin, A. Wang, Y. Guo, Y. Ding, Y. Guo, L. Wang, W. Zhan and F. Gao, *ACS Omega*, 2019, **4**, 9542–9551.
56 Y. Zhang, P. Wang, J. Yang, S. Lu, K. Li, G. Liu, Y. Duan and J. Qiu, *Carbon N. Y.*, 2021, **177**, 344–356.
57 A. Sousa, D. Mateo, L. Garzon–Tovar, K. Brennan, A. Rendón–Patiño, N. Morlanés, X. Wang, J. C. Navarro, J. Ruiz–Martinez, M. García–Melchor and J. Gascon, *Small*, 2025, **21**, 2411468.
58 R. K. Henderson, C. Jiménez-González, D. J. C. Constable, S. R. Alston, G. G. A. Inglis, G. Fisher, J. Sherwood, S. P. Binks and A. D. Curzons, *Green Chem.*, 2011, **13**, 854.
59 C. M. Alder, J. D. Hayler, R. K. Henderson, A. M. Redman, L. Shukla, L. E. Shuster and H. F. Sneddon, *Green Chem.*, 2016, **18**, 3879–3890.
60 D. Prat, A. Wells, J. Hayler, H. Sneddon, C. R. McElroy, S. Abou-Shehada and P. J. Dunn, *Green Chem.*, 2016, **18**, 288–296.
61 F. G. Delolo, L. Duarte Almeida, G. M. Vieira, E. N. dos Santos and E. V. Gusevskaya, *Green Chem.*, 2025, **27**, 4816–4866.
62 B. Liu, N. Huang, Y. Wang, X. Lan and T. Wang, *ACS Catal.*, 2021, **11**, 15235–15243.
63 B. Liu, Y. Sun, M. Li, Z. Fan, X. Chen, X. Lan, Q. Zhong and T. Wang, *ACS Catal.*, 2024, **14**, 15956–15964.
64 Y. Li and Q. Sun, *Adv. Energy Mater.*, 2016, **6**, 1600463.
65 Y. Liu, Q. Wang, J. Zhang, J. Ding, Y. Cheng, T. Wang, J. Li, F. Hu, H. Bin Yang and B. Liu, *Adv. Energy Mater.*, 2022, **12**, 2200928.